Capacitively Coupled Arrays of Multiplexed Flexible Silicon Transistors for Long-Term Cardiac Electrophysiology

Hui Fang[1,2,3†], Ki Jun Yu[2,3,4†], Christopher Gloschat[5†], Zijian Yang[2,3], Chia-Han Chiang[6], Jianing Zhao[2,3], Sang Min Won[2,3], Siyi Xu[2,3], Michael Trumpis[6], Yiding Zhong[2,3], Enming Song[2,3], Seung Won Han[2,3], Yeguang Xue[7], Dong Xu[2,3], Gert Cauwenberghs[8], Matthew Kay[5], Yonggang Huang[7], Jonathan Viventi[6], Igor R. Efimov[5*] and John A. Rogers[2,3*]

[1]*Department of Electrical and Computer Engineering, Northeastern University, Boston, MA 02115, USA*

[2]*Department of Materials Science and Engineering, University of Illinois at Urbana-Champaign, Urbana, IL 61801, USA*

[3]*Frederick Seitz Materials Research Laboratory, University of Illinois at Urbana-Champaign, Urbana, IL 61801, USA*

[4]*School of Electrical and Electronic Engineering, Yonsei University, Seoul, 03722, Republic of Korea*

[5]*Department of Biomedical Engineering, The George Washington University, Washington, DC 20052, USA*

[6]*Department of Biomedical Engineering, Duke University, Durham, NC 27708, USA*

[7]*Department of Mechanical Engineering and Department of Civil and Environmental Engineering, Northwestern University, Evanston, IL 60208, USA*

[8]*Department of Bioengineering, University of California San Diego, La Jolla, CA 92093, USA*

[†]*These authors are contributed equally to this work.*

**To whom correspondence should be addressed. E-mail: jrogers@illinois.edu or efimov@gwu.edu*

Supplementary Note 1-3

Supplementary Figure 1-25

Supplementary Movie 1-4

List of contents:

Supplementary Note 1: Step-by-step process flow to achieve flexible, capacitively coupled, active sensing electrode array.

Wafer back grinding

1. Start with SOI (Si device layer 200 nm, Box layer 1 µm, and handling Si 500 µm).
2. Grind the SOI wafer to 200 µm from back side by Syagrus Systems;
3. Cut the wafer into chips of device size.

Doping

4. RCA cleaning of SOI chips.
5. Dry thermal oxidation to form 200 nm SiO_2 at 1150 ^oC;
6. Photolithography to define S/D doping area using photoresist (PR) (AZ 5214E);
7. RIE to dry etch SiO_2, (a) 50 mTorr of CF_4/O_2 (40/1.2 sccm), with RF power 100 W for 5 min, (b) gentle O_2 plasma, 50 mTorr, 20 sccm of O_2, with RF power 100 W for 20 sec;
8. BOE (6:1) wet etch SiO_2 for 2 min;
9. PR strip by acetone, IPA and blow dry;
10. RCA cleaning;
11. Dope S/D area with diffusive phosphorus source at 1000 ^oC for 6 min;
12. Wet etch SiO_2 doping mask using 49% HF for 20 sec; and DI rinse.

Isolation

13. Photolithography to define Si isolation area using PR (AZ 5214E);
14. RIE to dry etch Si (50 mTorr, 40 sccm of SF_6, with RF power of 100 W for 1 min);
15. PR stripe by acetone, IPA and blow dry;

Gate stack deposition

16. RCA cleaning
17. Dry thermal oxidation to form 100 nm SiO_2 at 1150 ^oC.
18. Deposit 15 nm Al_2O_3 at 80 ^oC using an Atomic Layer Deposition (ALD) system;

Via 0

19. Photolithography to define S/D opening via using PR (AZ 5214E);
20. Gentle O_2 plasma using RIE (50 mTorr, 20 sccm of O_2, with RF power 100 W for 20 sec);

21. BOE (6:1) to etch gate dielectric for 3 min;
22. PR stripe by acetone soaking, IPA and blow dry;

Metal 1

23. Deposit Cr/Au, 5/100 nm with an e-beam evaporator;
24. Photolithography to define metal 1 using PR (AZ 5214E);
25. Au, Cr wet etching using Au, Cr etchant respectively;
26. PR stripe by acetone, IPA and blow dry;
27. Measure test transistors;

Interlayer PI 2545

28. Clean samples using acetone, IPA, DI, and blow dry;
29. Dehydration: bake samples at 110 ^{o}C for 5 min;
30. Spin coat PI adhesion promoter (VM 652) using 500 rpm 5s, hold 20s, 3000 rpm 30s; soft bake at 110 ^{o}C for 1 min;
31. PI coating: spin coat PI 2545 precursor at 4500 rpm for 30 sec; soft bake at 150 ^{o}C for 6 min; cure at 250 ^{o}C for 70 min;

Via 1

32. Photolithography to define via 1 using PR (AZ P4620);
33. RIE to etch Via 1 (200 mTorr, 20 sccm O_2, with RF power of 150 W for 15 min);
34. Check microscope and resistance to make sure via is open;
35. PR stripe by acetone, IPA, and blow dry;

Metal 2

36. Deposit Cr/Au, 10/500 nm with an e-beam evaporator;
37. Photolithography to define metal 2 using PR (AZ 5214E);
38. Au, Cr wet etching using Au, Cr etchant respectively ;
39. PR stripe by acetone, IPA and blow dry;

PI substrate 2545

40. Clean samples using acetone, IPA, DI, and blow dry;
41. Dehydration: bake samples at 110 ^{o}C for 5 min;
42. Spin coat VM 652 using 500 rpm 5s, hold 20s, 3000 rpm 30s; soft bake at 110 ^{o}C for 1 min;

43. PI coating: spin coat PI 2545 precursor at 3000 rpm for 30 sec; soft bake at 150 ^{o}C for 6 min; cure at 250 ^{o}C for 70 min;

Pre-conditioning before bonding

44. Deposit 20 nm Al_2O_3 at 150 ^{o}C to the devices' PI side using ALD;
45. Deposit Ti/SiO_2 5/20 nm to the devices' PI side with an e-beam evaporator;

Bonding

46. Bond devices to 13-μm kapton films (coated with Ti/SiO_2 5/20 nm) using a ~ 5-μm-thick PDMS layer. Do UV-Ozone treatment on PDMS surface right before bonding. Si-O-Si bonding need to be achieved on both sides of the PDMS layer to ensure good robustness;
47. Bond devices to handling glass substrates using 10:1 PDMS. Use vacuum desiccator to remove bubbles, and cure at 110 ^{o}C for 30 min;

Si wafer removal

48. Grind the back Si side briefly until the contamination on the back is gone;
49. Si back RIE etching (50 mTorr of SF_6/O_2, 40/3 sccm, with RF power 100 W. Do 6 runs of 30 min;
50. Deep RIE to continue etching back the devices, until all the back Si is etched;

Contact lead opening

51. Spin coat HMDS at 3000 rpm for 30sec, then bake at 110 ^{o}C for 1 min;
52. Photolithography to define zif contact region, using PR (AZ P4620);
53. RIE to dry etch SiO_2, (a). 50 mTorr of CF_4/O_2 (40/1.2 sccm), with RF power 200 W for 30 min, (b), gentle O_2 plasma, 50 mTorr, 20 sccm of O_2 with RF power 100 W for 20 sec;
54. BOE (6:1) to wet etch SiO_2 for 4 min;
55. Measure test transistors;
56. Remove PR using acetone, IPA and blow dry;

Laser cutting

57. Laser cut to define the device outline profile;
58. Peel off devices gently from handling substrates;
59. Stick the stiffener onto the device zif side under microscope; devices are then ready to be tested with the DAQ.

Supplementary Note 2: *In vivo* recording on a canine model using the flexible, capacitively coupled, active sensing electrode array (covered by a thermal SiO_2 layer).

Briefly, we performed *in vivo* measurements in an open chest canine preparation (Supplementary Fig. 14). A cocktail of midazolam, butorphanol, and ketamine anesthetized the animal. Isoflurane subsequently maintained surgical plane level anesthesia. A sternal thoracotomy opened the ribcage and exposed the thoracic cavity. An incision in the pericardium allowed access to the heart, while maintaining the structural support provided by the remainder of the pericardium. We placed the electrode array on the basal free wall of the left ventricle during sinus rhythm. We acquired data in two-minute intervals and subsequently analyzed.

Supplementary Note 3: *In vivo* recording of rat auditory cortex using the flexible, capacitively coupled, active sensing electrode array (covered by a thermal SiO_2 layer).

We made an *in vivo* recording of primary auditory cortex and surrounding areas in an anesthetized rat using the flexible, capacitively coupled, active sensing electrode array with 64 nodes (Supplementary Fig. 15). The array has the same circuit design as the 396-node device used in the *ex vivo* experiments with just fewer nodes. Auditory evoked potentials (AEPs) were recorded from the epidural surface in response to 13 tone frequencies that ranged between 500 Hz and 32 kHz in half-octave increments. Evoked-response signal-to-noise ratio, which measures variability of the 50 ms post-tone window with respect to baseline windows, was 5.0217 ± 0.2898 (mean ± S.E.M.), in good agreement with our previous results from passive electrode arrays[1]. A tonotopic map of the frequency eliciting the highest amplitude response at each site (i.e. best frequency) showed an expected dorsorostral-ventrocaudal oriented gradient of high to low frequencies[1,2]. A best frequency confidence value from 0-1 was computed by a cumulative distribution function evaluated with the sum of-squares of standardized z-scores of each site's tone responses[1]. Confidence, as depicted by the degree of color saturation in the tonotopic map, was higher for strongly responding sites and low for sites with little discernible response. Best frequency confidence (encoded by the color-saturation of the tonotopy heatmap) indicated strong AEPs at the majority of sites. Weakly responding sites were likely a result of non-auditory cortical areas and/or poor electrode contact with the epidural surface.

References

1. Insanally M et al. A low-cost, multiplexed μECoG system for high-density recordings in freely moving rodents. *J. Neural Eng.* 2016; 13(2): 026030.

2. Polley DB， Read HL， Storace DA， Merzenich MM. Multiparametric auditory receptive field organization across five cortical fields in the albino rat. *J. Neurophys.* 2007; 97(5):3621-38.

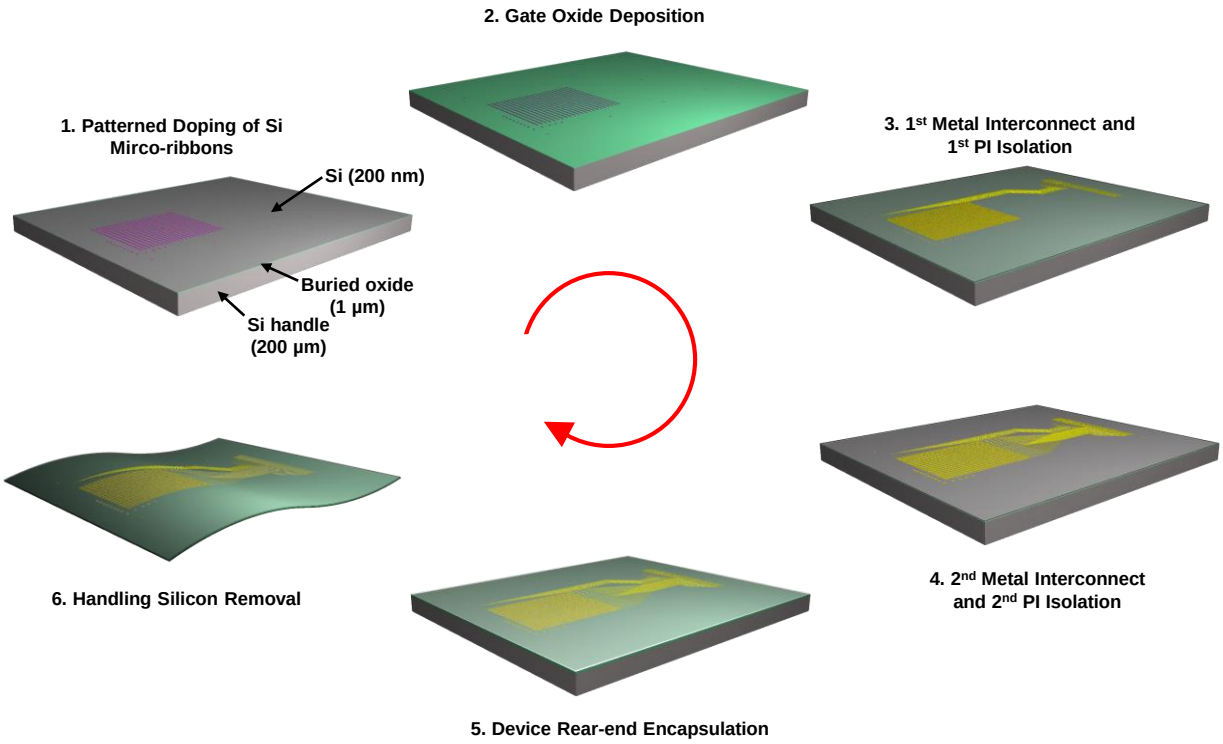

Supplementary Fig. 1. Procedures for fabricating flexible, capacitively coupled, actively multiplexed sensing matrix. From first to last: (1) Patterned doping of Si micro-ribbons on a SOI wafer; (2) Gate oxide deposition; (3) 1st metal interconnect and 1st Polyimide (PI) isolation; (4) 2nd metal interconnect and 2nd PI isolation; (5) Device rear-end encapsulation; (6) handling silicon removal. The buried oxide (Box) layer is then revealed on the front end of the device. The original Box thickness is 1 μm, ~ 100 nm of which is etched during the Si wafer removal process.

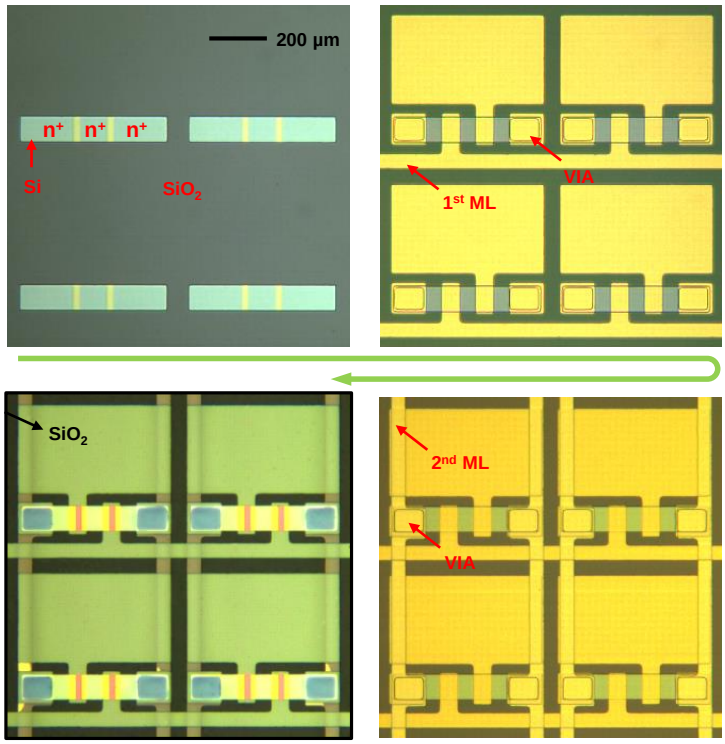

Supplementary Fig. 2. Images of four pixels within a device at various different key steps during the fabrication. From first to last: configuration after isolation of doped Si nanomembranes (Si NMs) in four unit cells; configuration after fabrication of the source, drain, gate sensing pads, and row electrodes for multiplexed addressing; configuration after second metallization, including the column output electrodes. Final layout of the device after removing the Si-handle-wafer removal, revealing the buried oxide (Box) layer as the tissue-contacting side.

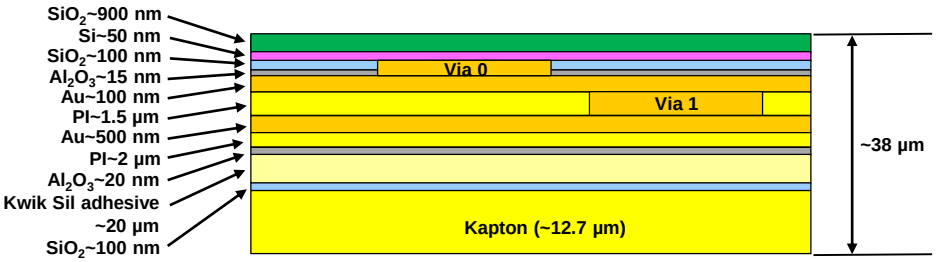

Supplementary Fig. 3. Illustration of the cross-section of the capacitively coupled, flexible active sensing matrix. The material and thickness for each layer is denoted.

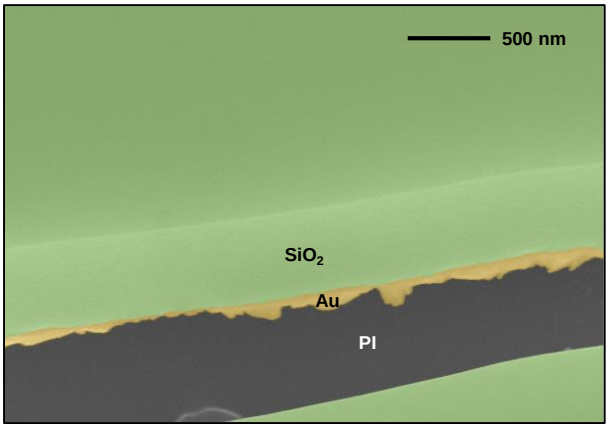

Supplementary Fig. 4. A 45^{o} tilted-view SEM image depicting the SiO_2, Au and PI interface in the final device.

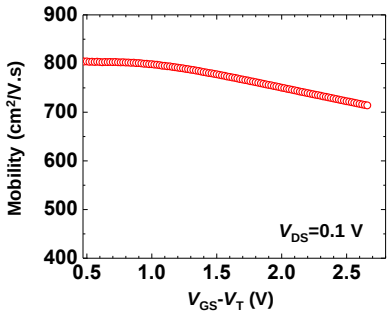

Supplementary Fig. 5. Effective mobility (μ_{eff}) as a function of gate voltage for the transistor in Fig. 1c, demonstrating the high performance of the Si active circuits. The high mobility leads to low output impedance from the source-following buffer circuit, and high switching speed from the multiplexing transistor.

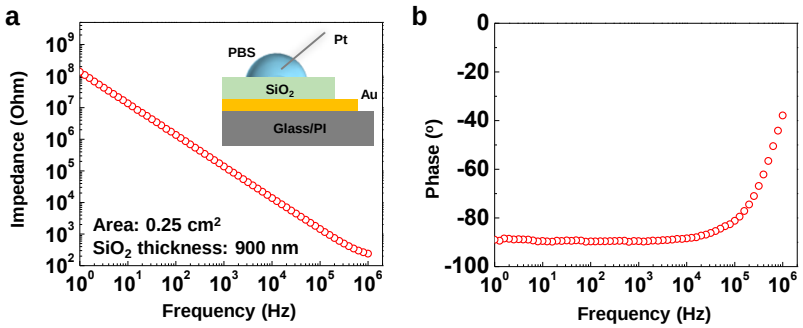

Supplementary Fig. 6. EIS characterization of the top SiO_2 layer on the electrode array. (**a**) Impedance and (**b**) phase as a function of frequency for a 900-nm SiO_2 layer with 0.25 cm^2 area. The electrode input impedance for each capacitively coupled sensing electrode (270 μm×460 μm) is calculated to be 2.6×10^9 Ω at 10 Hz. Inset in a: a schematic illustration of the cross-section of the EIS sample.

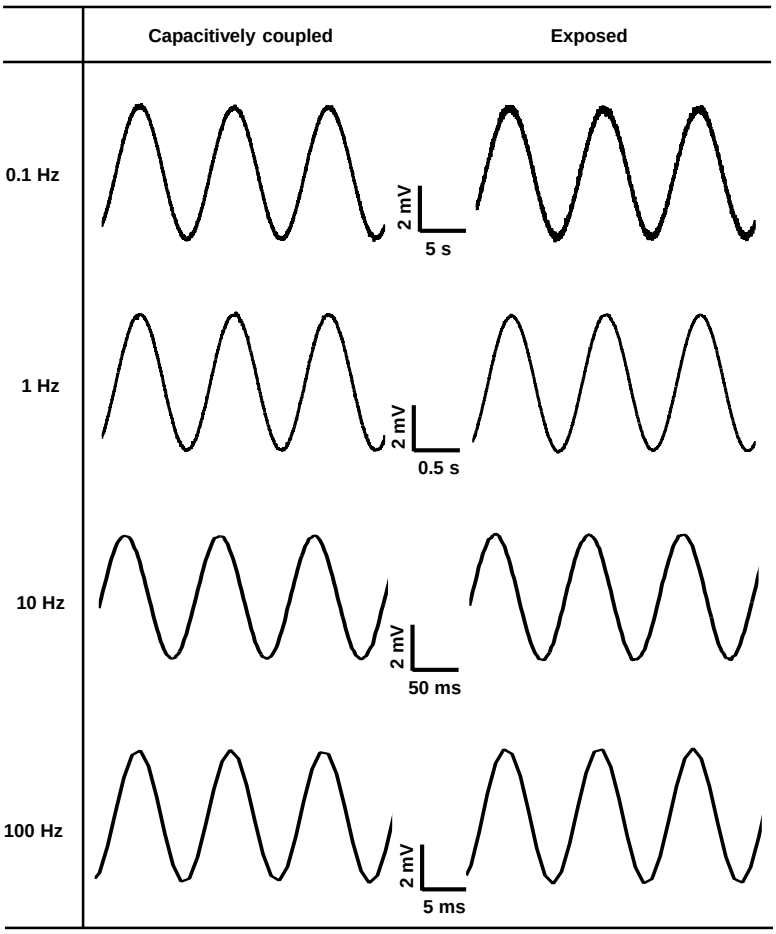

Supplementary Fig. 7. Comparison of electronic response with and without capacitive coupling from different input frequencies, demonstrating that capacitively coupled sensing electronics performed well over a wide dynamic range, with similar or better performance than exposed-metal electronic interface.

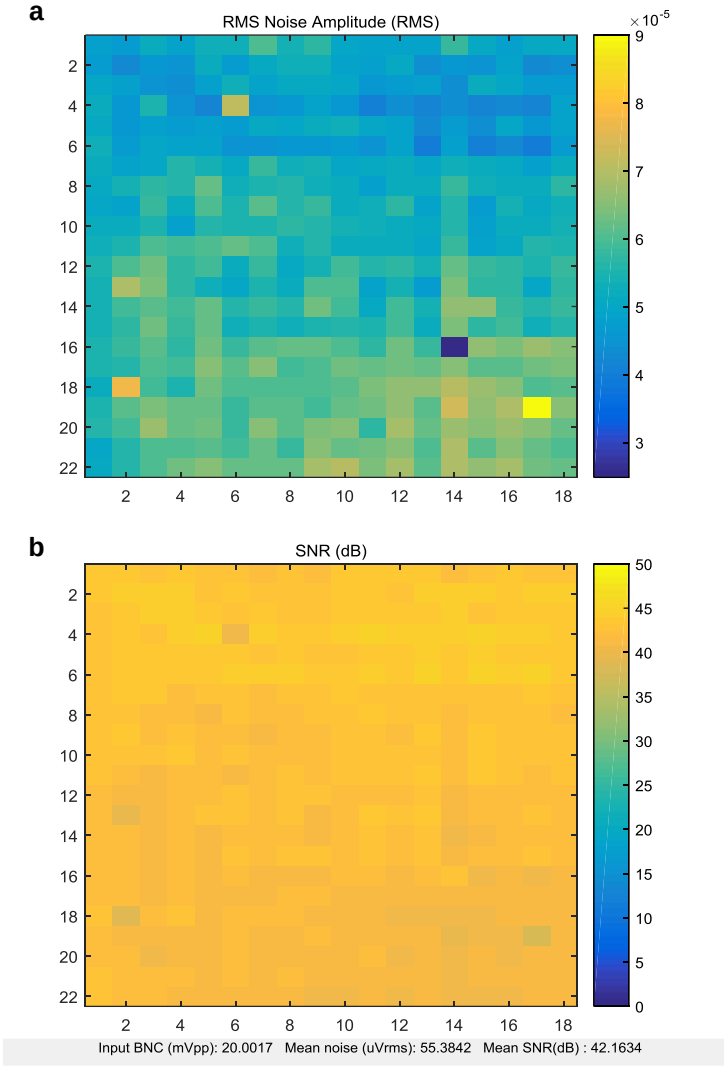

Supplementary Fig. 8. Color map illustrating the spatial distribution of (**a**) noise and (**b**) SNR of the electrode array in Fig. 1, demonstrating the low noise of the capacitively coupled sensing.

a

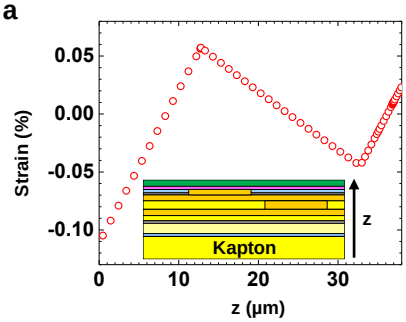

b

Material	Young's Modulus	Poisson's ratio
SiO_2	70 GPa	0.17
Si	130 GPa	0.27
Au	78 GPa	0.44
PI	2.5 GPa	0.34
Kwik Sil	1 MPa	0.49
Kapton	2.5 GPa	0.34

Supplementary Fig. 9. Strain distribution in the flexible electrode array. (**a**) Axial strain distribution along the thickness direction. Inset: schematic illustration of the array cross-section. (**b**) Material parameters in FEA simulations.

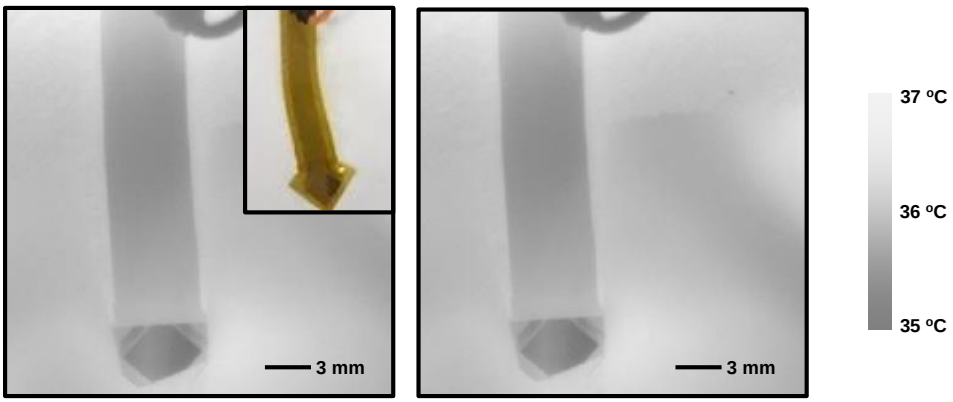

Supplementary Fig. 10. Infrared imaging of a capacitively coupled array of 252 nodes before (left) and after (right) 5 min recording, while resting on a hot plate at 37 ºC. The results indicate no apparent increase in temperature associated with operation of the device.

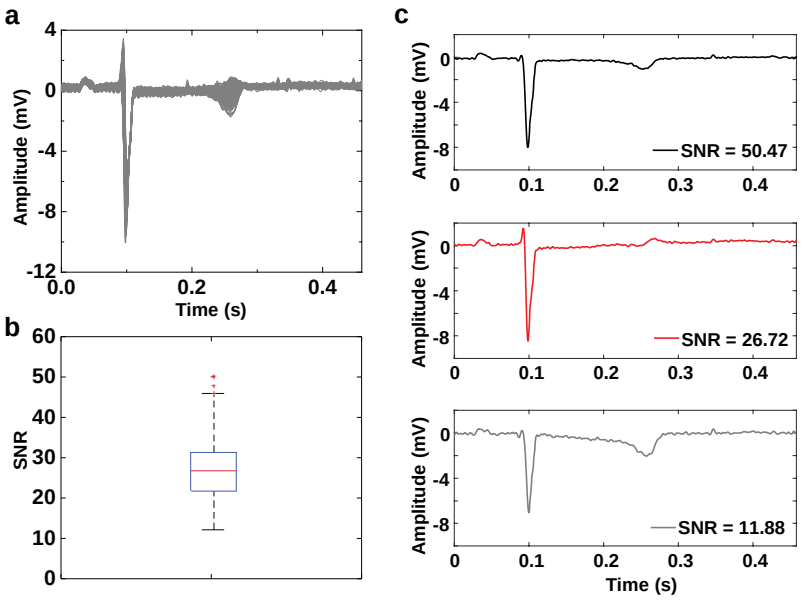

Supplementary Fig. 11. Noise analysis of recordings from all 396 channels from a flexible capacitively coupled sensing electronic system on a Langendorff-perfused rabbit heart. (**a**) Display of all 396 recordings. (**b**) Box plot showing the signal-to-noise ratio (SNR) range for the 396 recordings. (**c**) Display of the recordings with the highest, median, and lowest SNR.

Supplementary Fig. 12. Voltage traces from the same channel in the capacitively coupled sensing electronic system at the beginning and end of an *ex vivo* Langendorff perfused rabbit heart experiment. The amplitude and noise levels of the signal remain the same, demonstrating the stability of capacitive sensing over the entire course of the *ex vivo* experiment.

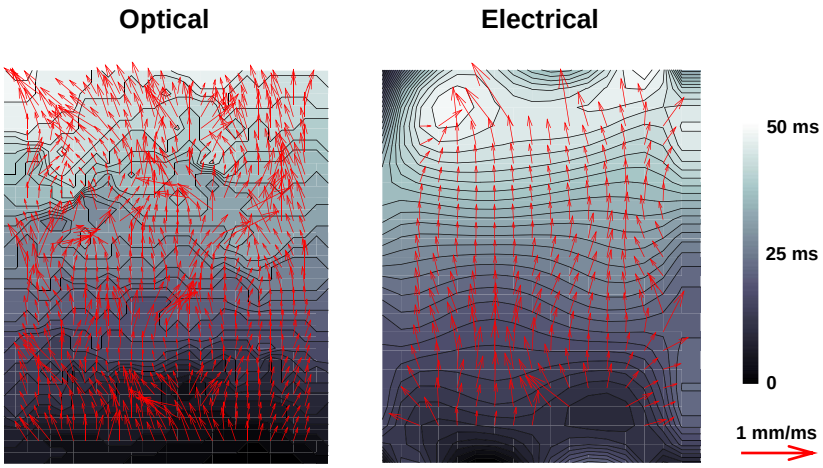

Supplementary Fig. 13. Calculated conduction velocity vector from optical and electrical maps at pacing of 300 ms cycle length. The magnitude of the red arrows indicates the amplitude of the velocity. The background maps are activation in grayscale.

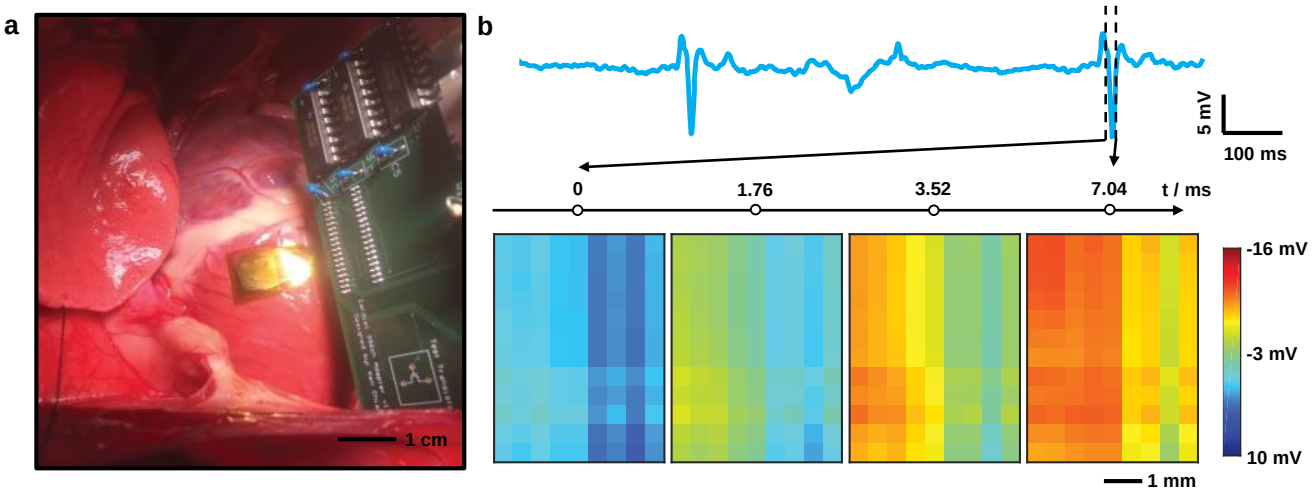

Supplementary Fig. 14. *In vivo* recording using a capacitively coupled sensing electronic system from a beating heart. (**a**) A photograph of a device laminated onto the left ventricle of a beating heart in an open chest experiment on a canine model. (**b**) Representative single voltage trace from the device (top), with representative voltage data map at four time points, showing normal cardiac wave-front propagation (bottom).

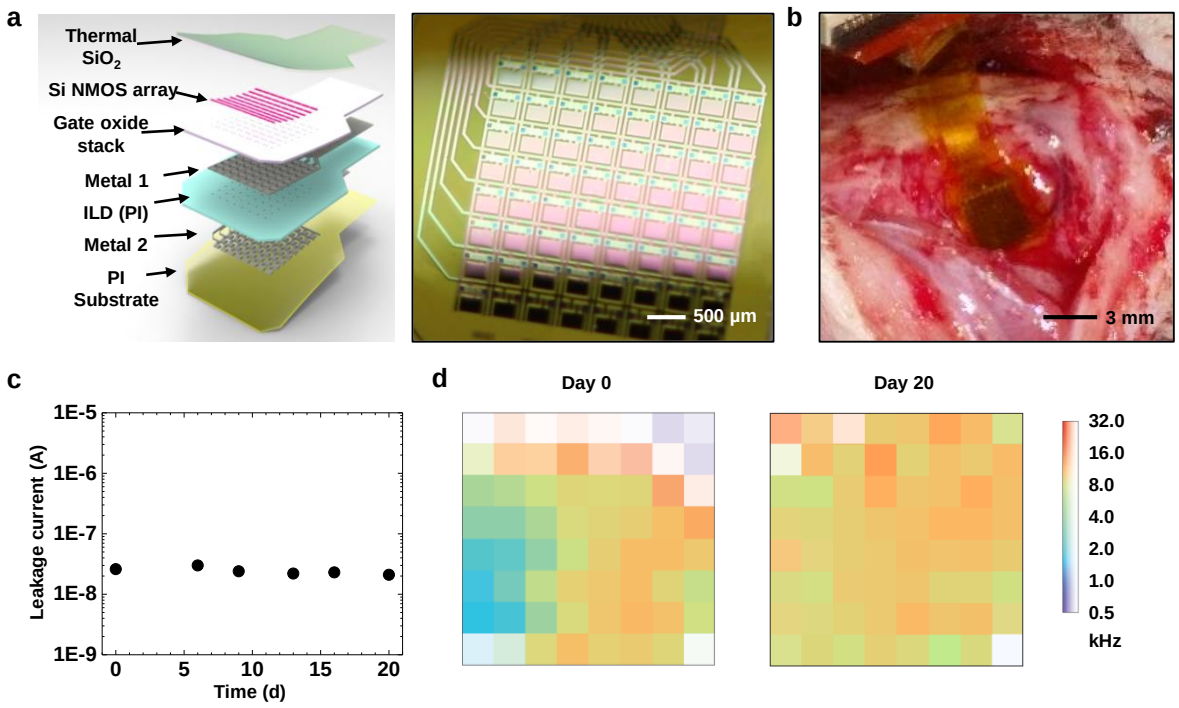

Supplementary Fig. 15. *In vivo* recording of rat auditory cortex using a flexible, capacitively coupled, actively multiplexed sensing matrix with 64 nodes. (**a**) Exploded-view schematic illustration (left) and a photograph (right) of a completed system in a slightly bend state. (**b**) Photograph of a device on the rat auditory cortex. (**c**) Leakage current measured from the array as a function of time, up to 20 days. (**d**) Map of best frequency revealed the dorsorostral-ventrocaudal gradient of representation in rat primary auditory cortex on day 0 (left) and day 20 (right), indicating stable sensing capabilities throughout the study.

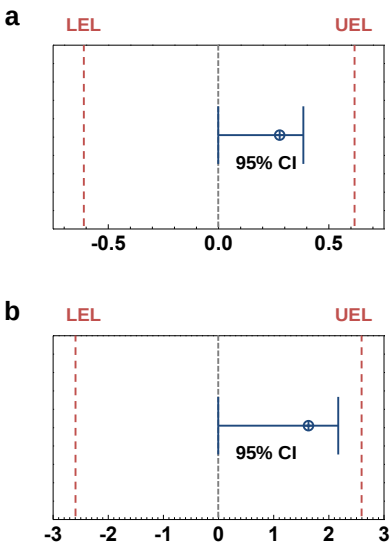

Supplementary Fig. 16. Sample equivalence test between the electrical and optical recordings. In order to demonstrate the accuracy of the bioelectric signals measured by the electrode a two sample equivalency test was performed using the electrode measurements as the test data and the optical measurements as the reference data. In the case of both (**a**) sinus rhythm (SR) and (**b**) 300 ms ventricular pacing, the isochronal maps of activation were found to be equivalent ($p < 0.05$) for both upper and lower bounds. Here the CI, LEL, UEL stand for confidence interval, lower equivalence limit and upper equivalence limit respectively.

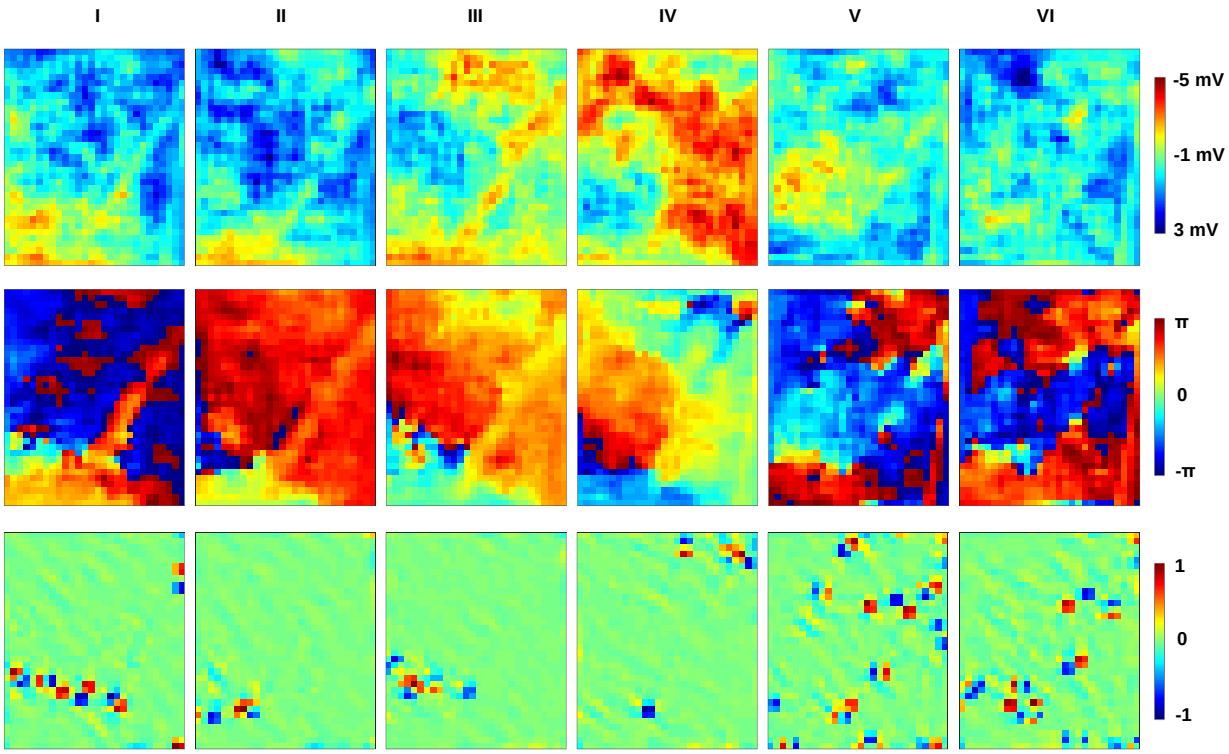

Supplementary Fig. 17. Optical signal (top row), phase (middle row), and phase singularity (bottom row) for ventricular fibrillation, corresponding to electrical mappings in Fig. 5.

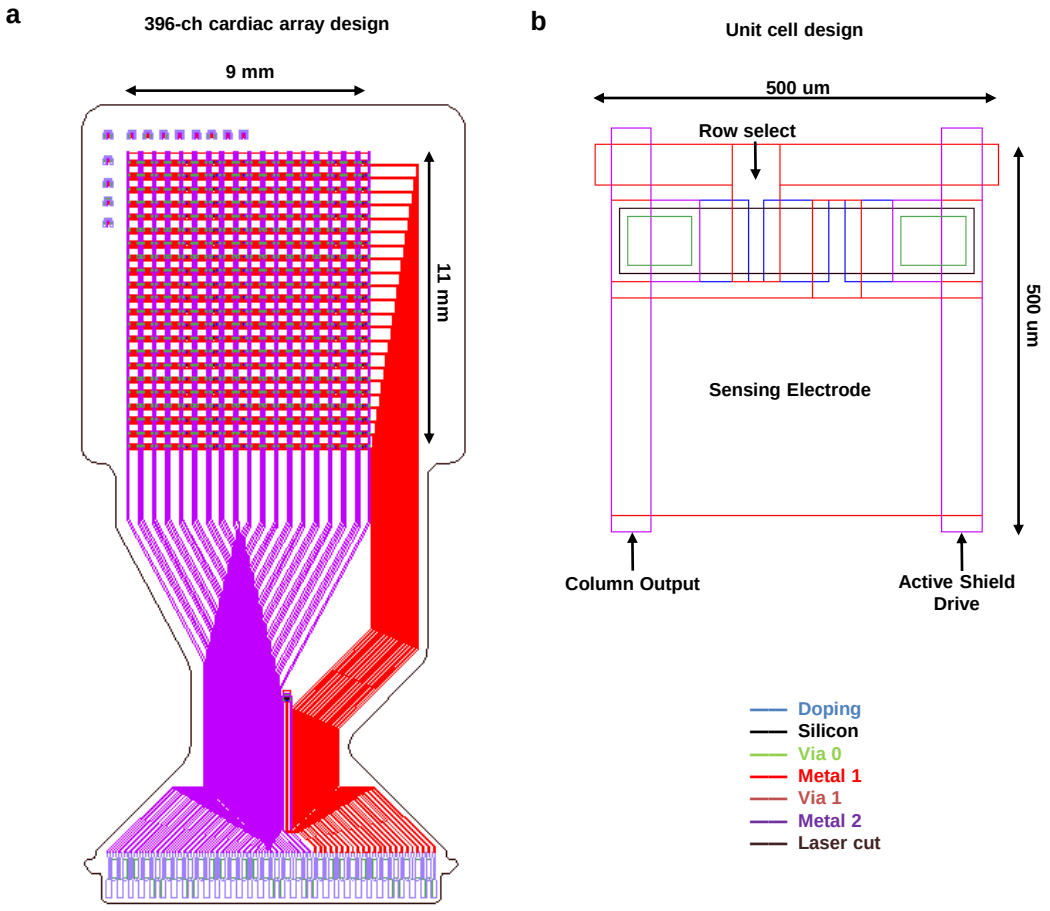

Supplementary Fig. 18. Schematic illustration of a 18×22 array of active multiplexed channels, showing (**a**) entire device and (**b**) unit cell design.

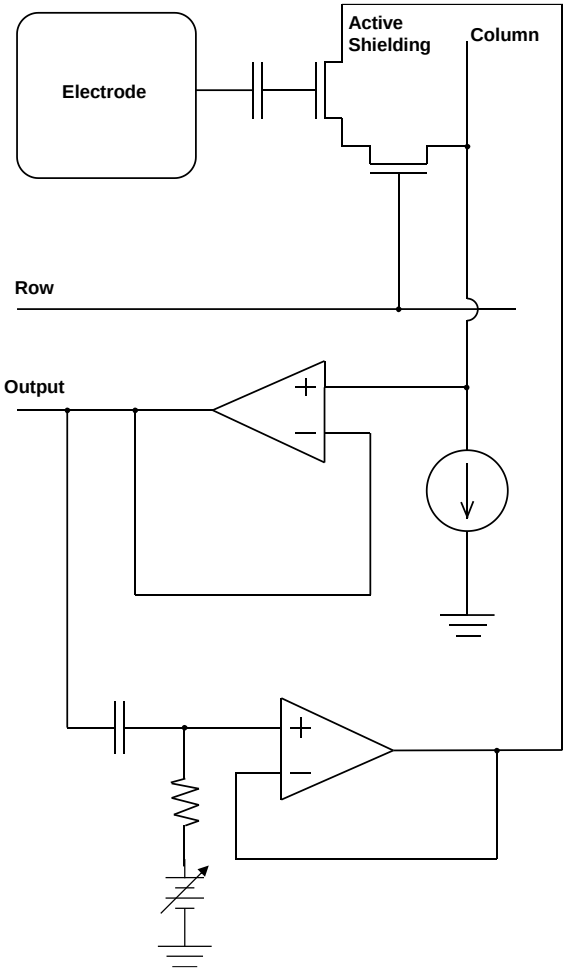

Supplementary Fig. 19. Schematic circuit diagram for the capacitively coupled, active multiplexed sensing electrode with an active shielding feedback.

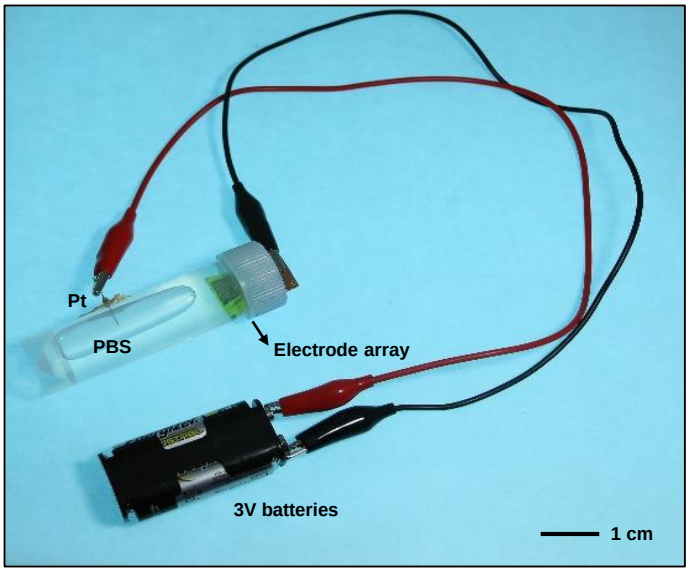

Supplementary Fig. 20. A Photograph of the set-up for soak testing of the electrode array. A sealed HDPE bottle was used to contain the phosphate buffered saline (PBS) solution, the electrode array and a Pt electrode. During the test the set-up was placed in a 37^{o}C oven and a 3 V DC bias was applied between the array and Pt electrode.

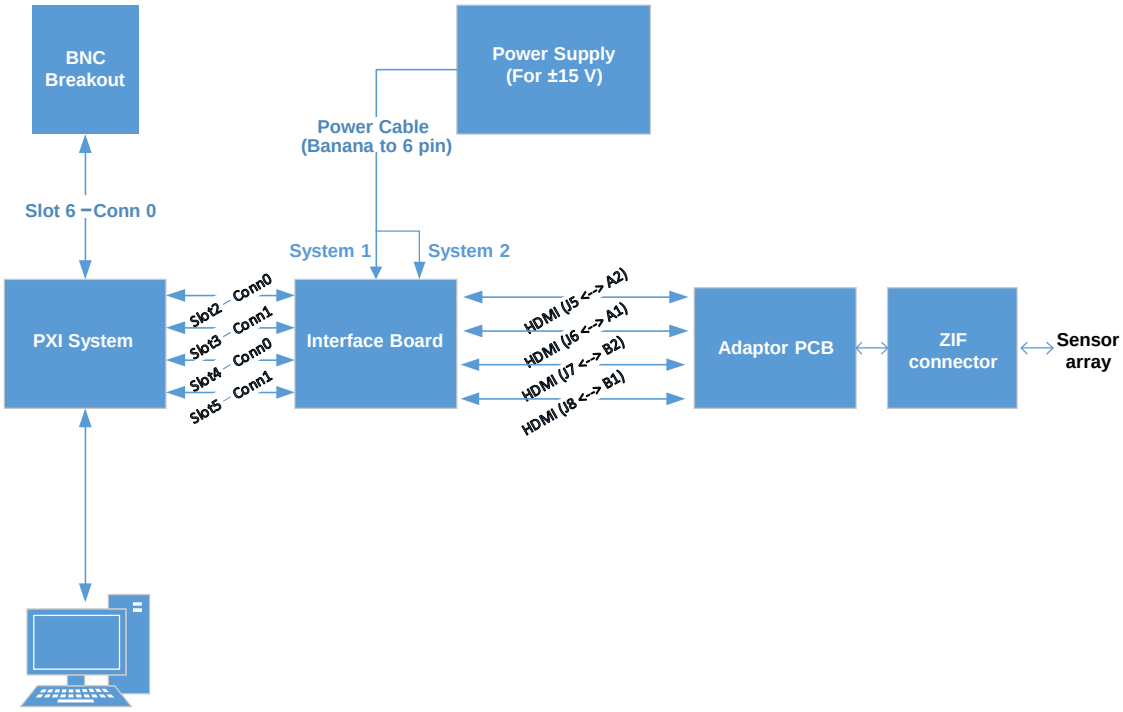

Supplementary Fig. 21. Schematic wiring diagram for the data acquisition system for sensing.

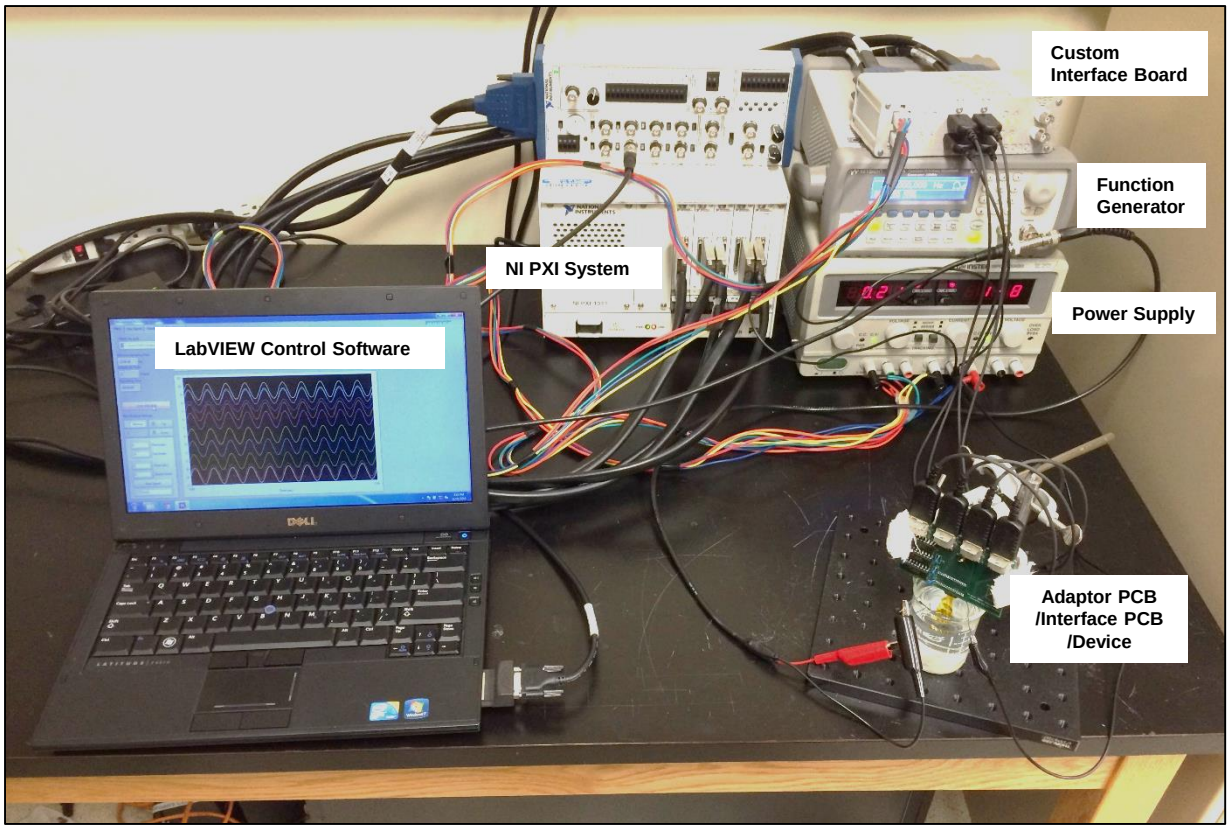

Supplementary Fig. 22. A Photograph of the data acquisition system with the electrode array during in vitro bench testing.

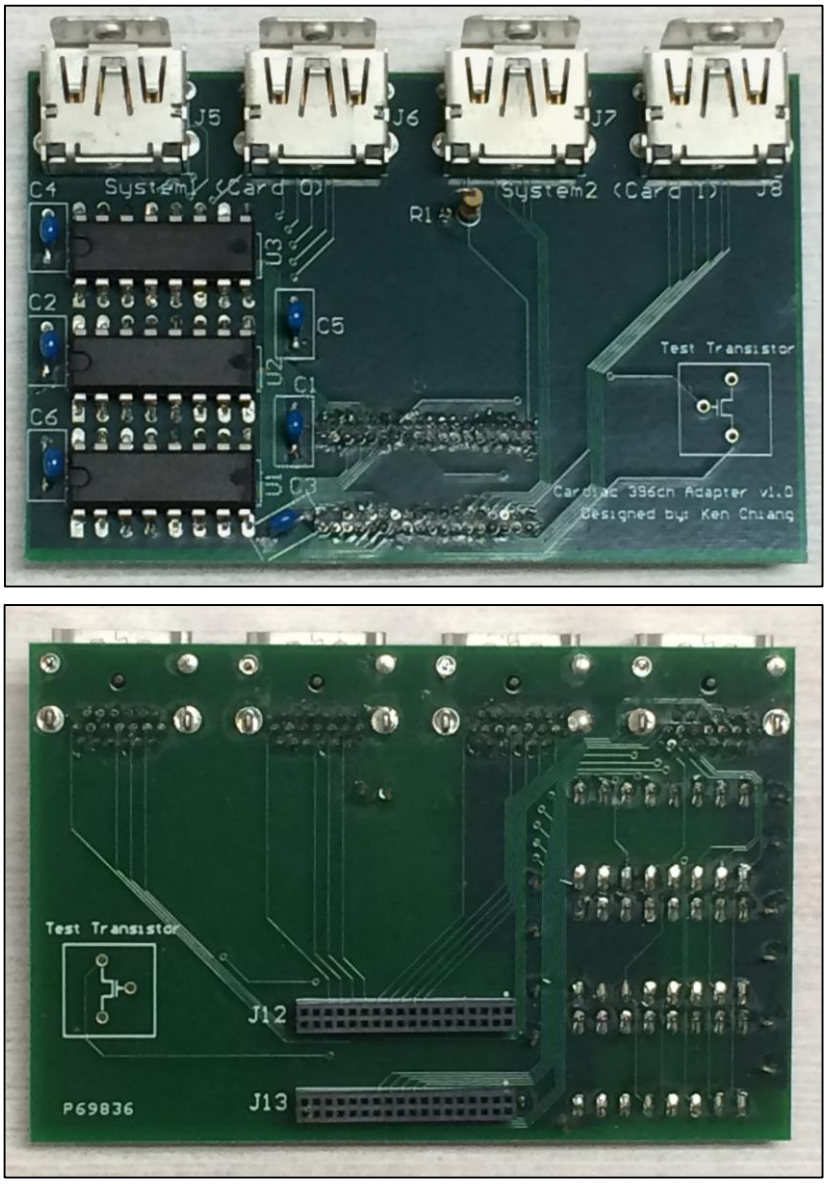

Supplementary Fig. 23. Photographs of the front (top) and back (bottom) side of the adaptor PCB board used between the electrode array and the DAQ system.

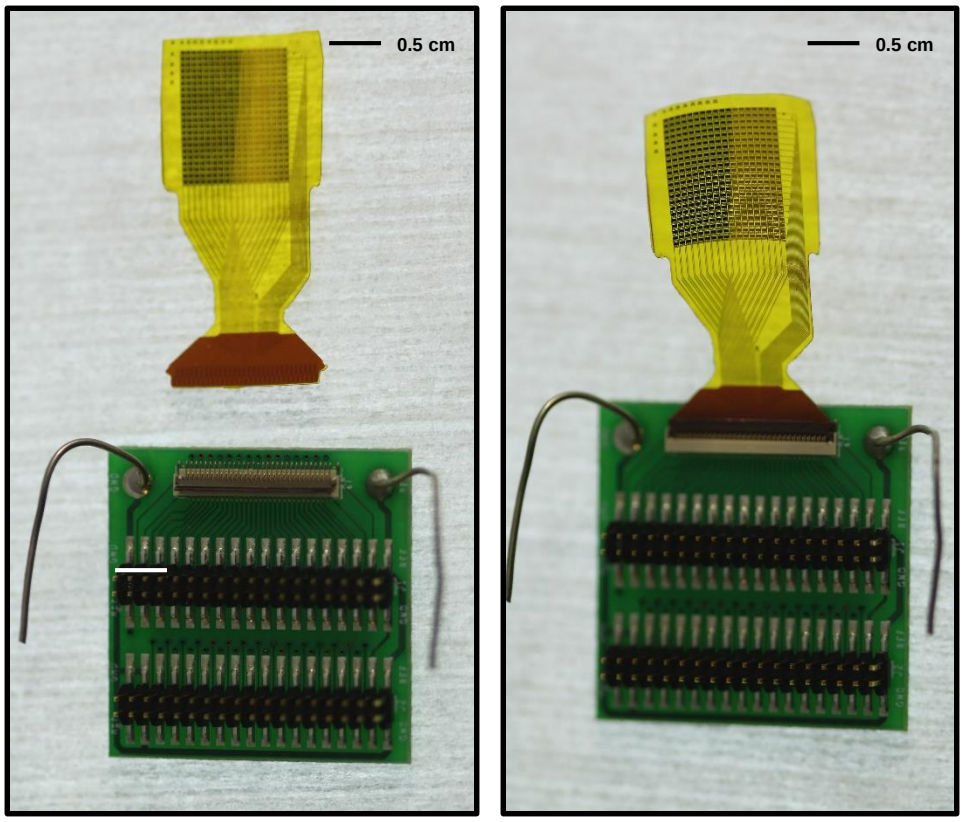

Supplementary Fig. 24. Photographs of an electrode array before (left) and after (right) being inserted into an interface PCB board through a zero-insertion-force (ZIF) connector.

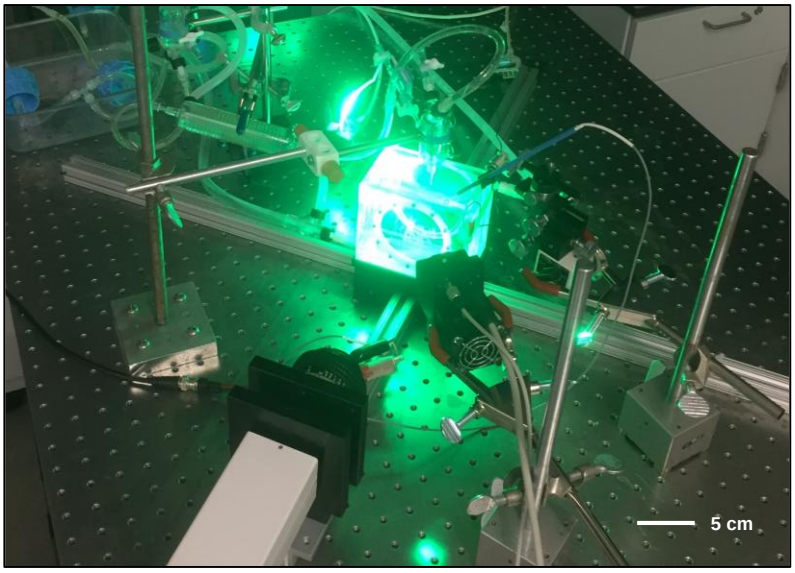

Supplementary Fig. 25. A photograph of the set-up for *ex vivo* recording on a Langendorff perfused rabbit heart model.

Supplementary Movie 1. A flexible capacitively coupled sensing electronic system on a Langendorff-perfused rabbit heart model.

Supplementary Movie 2. Voltage data from all electrodes illustrating the activation pattern of the heart during sinus rhythm.

Supplementary Movie 3. Voltage data from all electrodes illustrating the paced activation pattern moving from the apex to base.

Supplementary Movie 4. Voltage data from all electrodes illustrating the activation pattern of the heart during ventricular fibrillation.